nature communications

Article

https://doi.org/10.1038/s41467-025-66166-0

AI-powered SPOT imaging for enhanced myocardial scar detection and quantification

Received: 31 October 2024

Accepted: 29 October 2025

Aurelien Bustin[1,2,3], Matthias Stuber[1,3,4], Victor de Villedon de Naide[1,2], Manuel Villegas-Martinez[1,2], Kalvin Narceau[1], Thaïs Génisson[1], Théo Richard[1], Pauline Gut[1,3], Valery Ozenne[1], Marion Constantin[1], Guido Caluori[1], Konstantinos Vlachos[1], Géraldine Montier[2], Daphné Pasche[2], Théo Bedague[2], Jean-David Maes[2], Soumaya Sridi[2], Claire Bazin[2], Gaël Dournes[2], Stéphanie Clément-Guinaudeau[2], Ilyes Ben Lala[2], Méléze Hocini[1,5], Michel Montaudon[2], Pierre Jaïs[1,4] & Hubert Cochet[1,2]

Cardiovascular disease is the leading global cause of death, underscoring the need for accurate assessment of myocardial injury. The current gold standard, bright-blood late gadolinium enhanced MRI, suffers from poor contrast at the blood-scar interface, reducing sensitivity for subendocardial scar detection and limiting reproducibility. Moreover, reliance on expert manual analysis makes interpretation labor-intensive and variable. Here, we present SPOT, a multi-spectral bright- and black-blood imaging sequence that provides unprecedented scar-to-blood contrast and clear anatomical detail. Integrated with an artificial intelligence (AI) framework for automated image analysis, SPOT enables rapid, fully automated, and operator-independent quantification of myocardial injury. Validated in simulations, animal infarct models, and patients with heart disease, this combined imaging-AI platform delivers accurate detection and quantification in a single acquisition. This innovation presents significant opportunities for earlier diagnosis and enhanced therapeutic management of ischemic heart disease, with potential applications in a wide spectrum of other clinical settings.

Bright-blood phase-sensitive inversion recovery (PSIR) late gadolinium-enhanced (LGE) cardiac magnetic resonance (CMR) imaging is the current gold standard to assess and characterize myocardial injuries in patients[1]. On LGE images, scar presence and distribution are the cornerstone of the etiological diagnosis of structural heart diseases, and the transmurality of scar is employed to assess myocardial viability and to predict the benefit of subsequent revascularization[2,3]. Moreover, the burden and heterogeneity of scar on LGE images are also powerful predictors of ventricular arrhythmias, with the potential to significantly improve the primary prevention of sudden cardiac death with implantable cardioverter defibrillators[4,5]. Additionally, in patients with atrial or ventricular arrhythmias, LGE imaging allows for a non-invasive assessment of myocardial injuries both pre- and post-ablation and has proved to be an effective tool to assist catheter ablation procedures[6,7].

The strength of the bright-blood LGE technique lies in its ability to provide high contrast between the injured and viable myocardium, owing to an inversion-recovery mechanism that artificially blackens the healthy tissue in the images[1]. However, these clinical applications with direct impact on patient trajectories are all impaired by the poor

---

[1]IHU LIRYC, Heart rhythm institute, Université de Bordeaux–INSERM U1045, Pessac, France. [2]Department of Cardiovascular Imaging, Hôpital Cardiologique du Haut-Lévêque, CHU de Bordeaux, Pessac, France. [3]Department of Diagnostic and Interventional Radiology, Lausanne University Hospital and University of Lausanne, Lausanne, Switzerland. [4]Center for Biomedical Imaging (CIBM), Lausanne, Switzerland. [5]Department of Cardiac Electrophysiology, Hôpital Cardiologique du Haut-Lévêque, CHU de Bordeaux, Pessac, France. e-mail: aurelien.bustin@ihu-liryc.fr

contrast at the blood-scar interface, resulting in ambiguities, limited sensitivity for detecting subendocardial scars[8] and limited robustness in scar quantification[9], as this step heavily relies on accurate manual delineation of the endocardial border. This manual prerequisite demands significant time from medical professionals, averaging 20 min per dataset[10], and becomes particularly arduous in cases where scar patterns are intricately linked to the endocardial border, leading to increased operator variability[11]. Despite significant efforts to develop sophisticated, automated tools for rapid and comprehensive quantification of myocardial scars on bright-blood LGE images, successful integration into clinical practice remains challenging due to the aforementioned obstacles.

To overcome the issues observed with conventional bright-blood LGE imaging, several groups have introduced black-blood LGE imaging approaches[8,12–16]. These techniques have proved useful in uncovering scar patterns that may be otherwise confounded with blood signal. However, black-blood imaging also comes with its own weaknesses: because the signal is equally suppressed in both the blood pool and the healthy myocardium, there is a loss of anatomical information, which makes spatial localization and transmurality assessment of myocardial scars a challenging task[16]. In parallel, several studies have proposed intermediate gray-blood or dark-blood delayed enhancement that aim to partially suppress blood signal and improve scar-blood contrast while maintaining some myocardial-blood differentiation[12]. While easier to integrate into clinical workflows, these techniques often yield suboptimal contrast and fail to achieve complete suppression of blood signal, potentially limiting sensitivity in detecting subtle or subendocardial scars.

In this work, we propose to break away from conventional imaging to enable fully automated myocardial scar detection and quantification by combining a tissue-driven imaging sequence configuration on the one hand and AI-powered image processing approaches on the other. Specifically, we propose an imaging pipeline that drastically removes ambiguity:

i) In image interpretation by allowing the separate optimization of scar contrast and scar localization with a joint bright- and black-blood LGE imaging sequence (SPOT), resulting in improved myocardial scar visualization.
ii) In scar quantification by leveraging the complementary information from both bright- and black-blood images with AI-based segmentation methods, resulting in fully automated and robust myocardial scar analysis.

This imaging pipeline was implemented, optimized, and validated through numerical simulations, phantom studies, and animal models of myocardial scars. Its feasibility, generality, and preliminary clinical performance were rigorously trained and tested in 450 patients with known or suspected ischemic heart disease. Our results demonstrate that robust myocardial scar imaging and quantification can be achieved without any manual interaction, representing a significant advancement in cardiac imaging.

Results

A schematic of the proposed SPOT image acquisition, segmentation, and scar analysis processes is illustrated in Fig. 1 and Supplementary Fig. 1.

Simulation experiment results

Figure 2a shows the extended phase graph (EPG) simulation outcomes that were used to guide subsequent in vivo acquisitions. For black-blood imaging, the combination of an inversion pulse alongside a T1-rho preparation module validated the near-complete suppression of both viable myocardium and blood signals, where their zero planes intersect, at a T1-rho duration of 27 msec. At this intersection point, viable myocardium and blood signals are effectively nulled while the scar signal remains positive. For bright-blood imaging, the simulations indicated an optimal myocardium-blood contrast with a T1-rho duration around 50 msec.

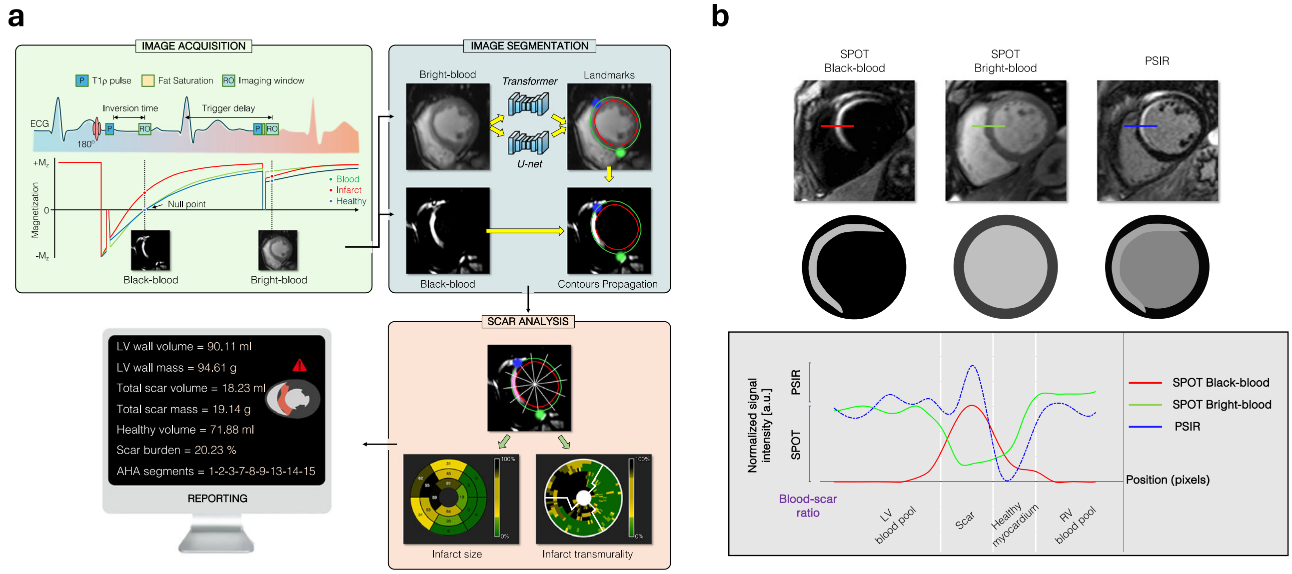

LV wall volume = 90.11 ml
LV wall mass = 94.61 g
Total scar volume = 18.23 ml
Total scar mass = 19.14 g
Healthy volume = 71.88 ml
Scar burden = 20.23 %
AHA segments = 1-2-3-7-8-9-13-14-15

Fig. 1 | Overview of the SPOT image acquisition, segmentation, and scar analysis processes. a SPOT collects 2D co-registered bright-blood and black-blood late gadolinium enhancement images in a single sequence. A transformer-based model is employed to fully automatically segment the left ventricular wall on bright-blood SPOT images, and a U-net is used to detect the two right ventricular insertion points. The segmented contours and identified landmarks are then propagated onto the black-blood images, facilitating detailed myocardial scar analysis, including the assessment of scar size and transmurality. The final reporting includes key metrics such as LV wall volume, scar volume, scar burden, and affected AHA segments. **b** Comparative short-axis SPOT and PSIR images collected in a patient with subendocardial septal scar, along with the signal evolution across the interventricular septum. The corresponding signal intensity profiles across the interventricular septum are illustrated, highlighting the superior blood-scar contrast achieved with SPOT black-blood imaging compared to PSIR. The schematic representations below each image depict the differential signal profiles and the relative effectiveness of each imaging sequence in distinguishing between blood pool, scar tissue, and healthy myocardium.

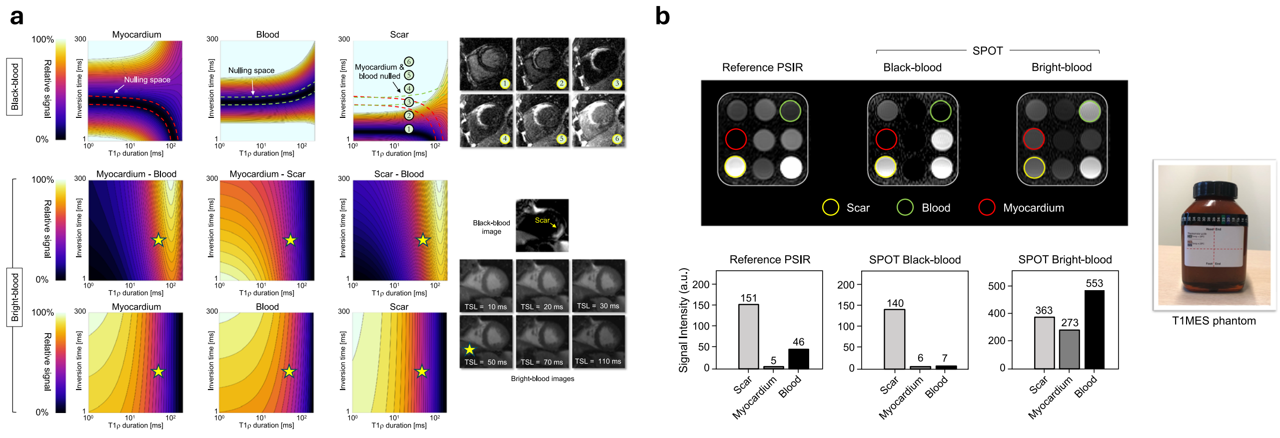

Fig. 2 | Extended phase graph simulations and phantom validation of SPOT imaging. a Simulations explore the interaction between inversion time and T1-rho pulse duration on signal dynamic and contrast enhancement of myocardium, blood, and scar tissues. The top panel illustrates simulations for odd heartbeats (black-blood image), revealing an optimal nulling of both blood and healthy myocardium signals achieved with a T1-rho duration of 27 msec. The bottom panel displays simulations for even heartbeats (bright-blood image), showcasing a favorable myocardium-blood contrast achieved with a T1-rho duration of 50 msec. The panels to the right show representative black-blood and bright-blood images illustrating the effects of varying T1-rho durations on myocardial scar visibility. **b** Results from the T1MES Phantom experiment comparing conventional bright-blood PSIR imaging with the proposed bright- and black-blood SPOT images. Signal intensities were measured in vials with T1/T2 values corresponding to post-contrast blood (green circle), viable myocardium (red circle), and scar tissues (yellow circle). Conventional PSIR imaging effectively suppresses the signal from the viable myocardium compartment but fails to suppress the blood signal, resulting in limited scar contrast. In contrast, the black-blood SPOT image demonstrates clear signal attenuation in both blood and viable myocardium compartments, yielding superior scar-to-myocardium and scar-to-blood contrasts. Signal intensity measurements further corroborate these observations, with distinct differences observed across the three imaging modalities shown in the lower panel.

Phantom experiment results

EPG-guided parameters were further tested in phantoms, as illustrated in Fig. 2b. Results confirmed that the black-blood sequence effectively eliminates both blood and myocardial signals simultaneously while highlighting scar tissue, and that the bright-blood sequence provides robust contrast between blood and myocardium. As anticipated, the conventional bright-blood PSIR sequence efficiently nulled viable myocardium signals, albeit leaving blood signal unaffected.

Animal experiment results

Selected SPOT images acquired at 1.5-T from two distinct ovine models, imaged three months post myocardial infarction and post-radiofrequency ablation, respectively, are presented in Fig. 3. The images are juxtaposed with slice-matched Masson trichrome histology and corresponding gross pathology images. Notably, PSIR imaging demonstrated a conspicuous lack of contrast for scar tissue adjacent to the blood pool, an issue effectively addressed by SPOT imaging. There was a high spatial concordance between SPOT and ex vivo images regarding the localization of myocardial injuries, which was confirmed at post-mortem dissection on gross pathology images. Furthermore, Masson trichrome staining revealed extensive replacement fibrosis within infarcted myocardial tissue or mature ablation lesions, thereby validating the observed hyperintensity on SPOT images.

Patient experiment results

Population. A flow diagram illustrating patient recruitment is provided in Supplementary Fig. 2. From a total of 516 patients meeting eligibility criteria, 66 patients (13%) were excluded: 37 due to residual motion artifacts, 23 due to suboptimal image contrast, and 6 due to incomplete heart coverage. Image quality issues in excluded patients are analyzed in Supplementary Fig. 3. A comparable number of patients were affected by artifacts on PSIR and SPOT images (46 vs. 57, $P = 0.253$). Examples of typical artifacts found on SPOT images are shown in Fig. 4a. The final study cohort comprised 450 patients with known or suspected ischemic heart disease (21% female, mean age 62.0 ± 11.7 years). Baseline characteristics are detailed in Supplementary Fig. 4.

Acquisition and processing time. The median scanning time across the cohort with SPOT was 4 min 30 s [IQR 4 min 30 s–4 min 50 s]. Manual segmentation of left ventricular (LV) wall and quantification of myocardial scar from SPOT images required an average of 20 min per dataset. In contrast, automated segmentation of the LV wall and landmark detection were performed in under 3 s per dataset, while scar segmentation took merely half a second per dataset, resulting in a total processing time of less than 4 s per dataset.

Accuracy of myocardial wall segmentation. LV wall segmentation reproducibility is analysed in Supplementary Fig. 5. Overall DICE scores indicated higher reproducibility for basal slices as compared to apical slices, both for SPOT and PSIR. Intra- and interobserver DICE scores for LV wall segmentation were consistently superior for SPOT images across apical, middle, and basal slices, as compared to PSIR images. The overall DICE score between manual and automated LV wall segmentation on SPOT images was 78.5% (IQR 76.4–81.2). Examples of automated LV wall segmentations are shown in Fig. 4b for six patients.

Accuracy of right ventricular insertion points. The method for detecting right ventricular insertion points is illustrated in Fig. 4c. The model yielded high confidence scores for both anterior and posterior right ventricular insertion points, indicating robust performance. No statistically significant differences were observed between anterior and posterior insertion points concerning Euclidian distance ($P = 0.295$) and angle ($P = 0.924$) when compared to manually identified reference points.

Signal intensities in patients. Signal intensities across scar, myocardium and blood regions are analyzed in Fig. 4d. While PSIR efficiently suppressed myocardium signal, no statistically significant difference was observed between scar and blood signals ($P = 0.171$). Conversely, black-blood SPOT imaging demonstrated equal attenuation of blood and myocardium signals ($P = 0.125$), with a notable difference between scar and myocardium and blood signals ($P < 0.001$ for both).

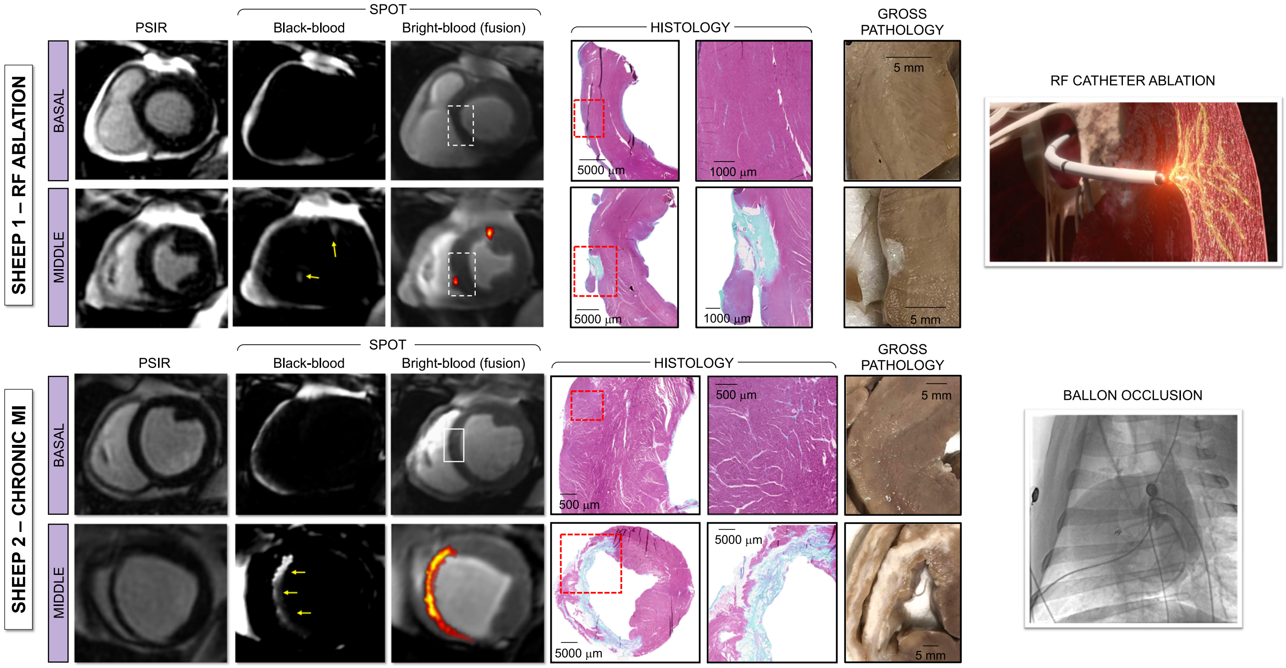

Fig. 3 | Comparative analysis of SPOT imaging with histology and gross pathology in animal models. This figure presents a comprehensive comparison of phase-sensitive inversion recovery (PSIR), SPOT imaging, Masson trichome histology, and gross pathology in two distinct ovine models of myocardial injury. Top row: imaging results from a sheep model subjected to multiple radiofrequency ablations, mimicking microinfarctions. The PSIR images show limited contrast in delineating the ablation sites, while the SPOT black-blood images enhance the visibility of the scar tissue. The bright-blood fusion images further improve the localization of the scar, with clear demarcation observed in the corresponding histology and gross pathology sections. This experiment was performed in one sheep. Scale bars: histology (left) 5000 µm, histology (right) 1000 µm, gross pathology 5 mm. Bottom row: imaging results from a sheep model with a large myocardial infarction induced by ischemia-reperfusion via balloon occlusion. The PSIR images again show suboptimal contrast for scar detection. In contrast, SPOT black-blood images provide superior scar delineation, while the bright-blood fusion images accurately localize the infarcted regions. These imaging results are validated by the corresponding histology and gross pathology, which reveal extensive fibrosis in the infarcted myocardium. This experiment was performed in one sheep. Representative data are shown; experiments were conducted in two sheep in total. Scale bars: histology (left) 500–5000 µm (depending on panel), histology (right) 500–5000 µm (depending on panel), gross pathology 5 mm. Arrows highlight myocardial injuries. MI myocardial infarction, RF radiofrequency.

Myocardial scar quantification

Scar segmentation techniques. The proposed automated region growing algorithm exhibited the highest DICE score at 82.0% (95% CI [78.7; 87.6]), contrasting with the full width at half maximum (FWHM) method's lowest score of 47.5% (95% CI [38.9; 64.2]). Confidence intervals were narrower for the region growing algorithm (Fig. 4e). Optimal performance for the region growing algorithm was achieved with a region growing distance (ε) of 0.15.

As shown in Supplementary Fig. 5, intraobserver and interobserver reproducibility for SPOT was consistently higher than PSIR for scar segmentation. In particular, in patients with subendocardial injuries (defined as scar transmurality ≤50%), SPOT maintained high agreement: intraobserver DICE score 84.3% [80.5–90.8], interobserver DICE score 73.5% [66.2–77.8], and automated vs. manual DICE score 80.4% [70.7–83.3], all substantially outperforming PSIR.

Visual comparisons of segmentation quality for seven techniques are shown in Fig. 5a, b derived from analyses conducted on five patients with myocardial infarction. A whole ventricle view of SPOT and PSIR images collected in a 43-year-old male patient with myocardial infarction is shown in Fig. 5c. Illustrative SPOT images collected in patients are shown in Fig. 6. Examples demonstrating the challenges in drawing subendocardial and scar contours on reference PSIR imaging are depicted in Fig. 6a. Illustrative PSIR and SPOT images from the testing set collected on 12 patients with large and small myocardial scars are shown in Fig. 6b, c.

Scar detection across AHA segments. Scar detection across AHA segments using PSIR, manual SPOT and automated SPOT is analyzed in Supplementary Fig. 6. A total of 800 myocardial segments were analyzed on PSIR and SPOT images in the testing cohort. Scars were detected on both PSIR and SPOT in 44 patients (88%). Overall, SPOT imaging identified 45 (observer 1) and 47 (observer 2) more scarred segments than PSIR (11.2% increase, $P = 0.018$) and revealed a greater number of scar segments per patient as compared to PSIR (10 [IQR 6–11] vs. 11 [IQR 7–12], $P < 0.001$). All segments with scar on PSIR images were corroborated on SPOT. The agreement between observers and between methods for scar detection across AHA segments is analyzed in Supplementary Fig. 7. Manual processing of SPOT images showed excellent intraobserver (Cohen's kappa $\kappa = 0.96$, 95% CI [0.93, 0.98]) and interobserver agreement ($\kappa = 0.90$, 95% CI [0.88, 0.93]). Agreement between automated and manual processing of SPOT images was also excellent ($\kappa = 0.94$, 95% CI [0.91, 0.96]). Intra- and interobserver agreements were substantially lower when processing PSIR images (intraobserver $\kappa = 0.89$, 95% CI [0.87, 0.93]; interobserver $\kappa = 0.82$, 95% CI [0.78, 0.86]).

Scar quantification. The reproducibility of manual scar quantifications is analyzed in Supplementary Fig. 8. Manual processing of SPOT images demonstrated excellent intra- and interobserver reproducibility in scar volume quantification (intraobserver intraclass correlation ICC = 0.91 [95% CI 0.83; 0.95]; interobserver ICC = 0.89 [0.80; 0.94]) with minimal bias and narrow limits of agreement (intraobserver bias −0.99 ± 3.13 mL; interobserver bias −0.98 ± 3.09 mL). Manual processing of SPOT images also yielded excellent reproducibility for the quantification of scar extent (intraobserver ICC = 0.94 [0.88; 0.97]; interobserver ICC = 0.92 [0.86; 0.96]), and scar transmurality

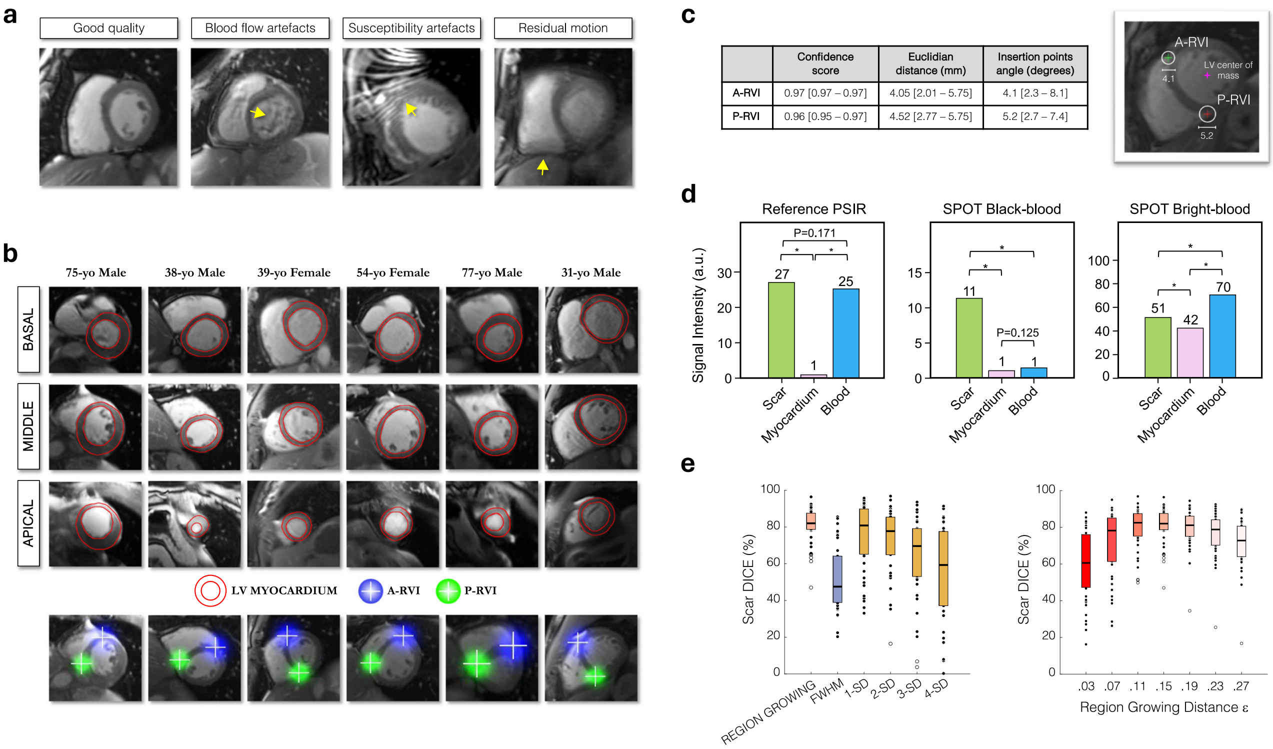

	Confidence score	Euclidian distance (mm)	Insertion points angle (degrees)
A-RVI	0.97 [0.97 – 0.97]	4.05 [2.01 – 5.75]	4.1 [2.3 – 8.1]
P-RVI	0.96 [0.95 – 0.97]	4.52 [2.77 – 5.75]	5.2 [2.7 – 7.4]

Fig. 4 | Evaluation of image quality, segmentation accuracy, signal intensities, and DICE scores. a Illustrative examples of artifacts observed in SPOT images. These artifacts primarily manifested as blood flow artifacts, predominantly affecting the basal slices. Additionally, susceptibility artifacts linked with balanced steady-state free-precession readouts were identified. Residual motion artifacts were also observed, particularly in patients experiencing challenges in maintaining consistent breath-holds. Artifacts are highlighted by arrows for clarity. **b** Automated left ventricular wall segmentation results and detected right ventricular insertion points on bright-blood SPOT images in six patients from the testing set. The segmentation outcomes demonstrate the ability of the automated pipeline to accurately delineate the left ventricle and reliably identify right ventricular insertion points (A-RVI and P-RVI), as depicted by the overlay of segmentation contours and landmarks. **c** Accuracy assessment of automatically detected right ventricular insertion points, reported as median values with interquartile ranges (25th–75th percentile). The reference point to compute the insertion points angle was the left ventricular center of mass. Two-sided Wilcoxon signed rank test. Confidence score, $P = 4.6 \times 10^{-6}$; Euclidian distance, $P = 0.295$; insertion points angle $P = 0.924$. A-RVI anterior right ventricular insertion point, P-RVI posterior right ventricular insertion point. **d** Comparative analysis of mean signal intensities obtained in scar, myocardium, and blood regions across the testing set cohort. Signal intensities were evaluated in reference PSIR images and proposed bright- and black-blood SPOT images ($N = 50$). The two-sided Wilcoxon signed rank test was employed to compare signal intensities between tissue types. Reference PSIR: scar versus blood: $P = 0.171$; scar versus myocardium: $P = 1.6 \times 10^{-8}$; blood versus myocardium: $P = 1.6 \times 10^{-8}$; SPOT black-blood: scar versus blood: $P = 2.4 \times 10^{-8}$; scar versus myocardium: $P = 2.4 \times 10^{-8}$; blood versus myocardium: $P = 0.125$; SPOT bright-blood: scar versus blood: $P = 5.9 \times 10^{-8}$; scar versus myocardium: $P = 6.9 \times 10^{-3}$; blood versus myocardium: $P = 2.4 \times 10^{-8}$. **e** Comparison of myocardial scar segmentation techniques for black-blood SPOT imaging using the DICE index, $n = 44$ independent patients. (Left) Comparison of segmentation performance between the full width at half maximum (FWHM) method, various n-SD approaches ($n = 1$–4) and the region growing technique against manual segmentation for infarct size quantification on black-blood SPOT images. For the n-SD segmentation method ($n = 1$–4), the reference signal was manually extracted from a region-of-interest delineated in the remote (non-infarcted) myocardium. The starting seed point for the seeded region growing algorithm was automatically determined by the left ventricular center of mass, eliminating the need for user interaction. (Right) Multiple region growing distances ε were evaluated to optimize the accuracy of infarct delineation. Box plots display the 25th and 75th percentiles (bounds of the box), with the center line indicating the median (50th percentile). Whiskers extend to the minimum and maximum values, and individual points represent outliers. Source data are provided as a Source data file.

(intraobserver ICC = 0.98 [0.96; 0.99]; interobserver ICC = 0.94 [0.90; 0.97]). Manual processing of PSIR images yielded comparable correlation between measurements, albeit with substantially larger intra- and interobserver mean differences (bias).

Agreement between methods for scar quantifications is analyzed in Supplementary Fig. 9. Agreement between automated and manual scar quantifications on SPOT images was excellent for scar volume (ICC = 0.90 [0.82; 0.95], bias −1.1 ± 3.3 mL), scar extent (ICC = 0.89 [0.79; 0.94], bias −2.3 ± 7.0%), and scar transmurality (ICC = 0.97 [0.95; 0.98], bias −1.0 ± 6.5%). Agreement between manual SPOT and manual PSIR processing was good for scar volume (ICC = 0.77 [0.59; 0.87], bias +2.7 ± 4.6 mL), and excellent for scar extent (ICC = 0.85 [0.74; 0.92], bias +2.1 ± 8.3%) and scar transmurality (ICC = 0.97 [0.95; 0.98], bias −2.6 ± 6.7%).

To further characterize the nature of the additional LGE segments detected with SPOT, we analyzed the transmurality distribution of identified segments for both SPOT and PSIR (Supplementary Fig. 10). SPOT yielded a greater number of segments across most transmurality grades, with the largest relative increases observed in the subendocardial (1–25%) and mid-wall (26–50%) ranges, highlighting its improved sensitivity in detecting both subendocardial and intermediate-grade injuries.

The distribution of scar across AHA segments in the test cohort with PSIR, manual SPOT, and automated SPOT is shown in Fig. 6d. Selected images underscoring the value of SPOT in alleviating scar-blood contrast ambiguities are shown in Fig. 6a. Results of SPOT imaging in large and small scars are shown in Fig. 6b, c, respectively.

Discussion

Accurate identification of myocardial injury via non-invasive CMR holds pivotal diagnostic and prognostic significance across various cardiomyopathies, deeply influencing therapeutic decisions. Scar

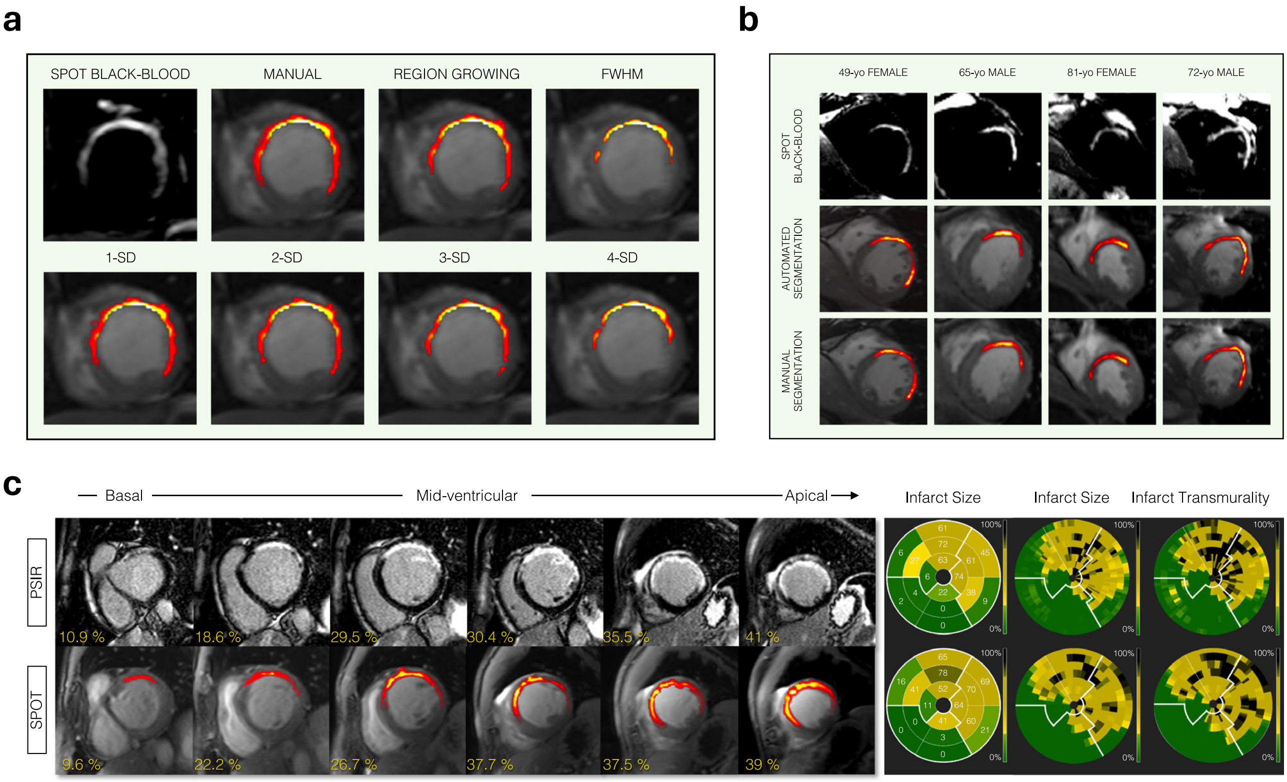

Fig. 5 | Comparative scar segmentation results and whole ventricle visualization in patients with myocardial infarction. a Comparison of full width at half maximum (FWHM), *n*-SD (*n* ranging from 1 to 4) and the region growing technique against manual segmentation for infarct size quantification. The overlay of segmentation contours on the SPOT images illustrates the variability and accuracy of each method in delineating the infarcted regions. **b** Comparison of automated segmentation using a seeded region growing algorithm against gold standard manual segmentation across four patients of varying ages and genders. The top row shows black-blood SPOT images, followed by automated segmentation results in the middle row, and manual segmentation outcomes in the bottom row. **c** Whole ventricle visualization of myocardial scar in a 43-year-old male patient with myocardial infarction originating from the left anterior descending artery. The figure compares SPOT and PSIR images, providing a slice-by-slice assessment of scar extent as a percentage of left ventricular mass. The corresponding bullseye plots illustrate the infarct size and transmurality across different segments of the left ventricle.

presence and distribution on LGE images are essential for diagnosing structural heart diseases, while scar transmurality serves as a vital parameter for evaluating myocardial viability in ischemic patients, guiding subsequent revascularization decisions. Additionally, the burden and heterogeneity of scar on LGE images are potent predictors of ventricular arrhythmias, potentially transforming the primary prevention of sudden cardiac death through implantable cardioverter defibrillators. In ischemic heart disease, this task presents some challenges. The presence of subendocardial LGE foci, located at the blood-myocardium interface, complicates interpretation of bright-blood PSIR LGE images due to inadequate contrast between the blood pool and scar tissue. Consequently, precise evaluation of scar location, transmurality, and size using established bright-blood LGE sequences is subjective and demands laborious efforts and extensive clinical expertise and heavily relies on the accurate delineation of the endocardial border. The lack of automation decreases clinical accuracy, increases workload, and leads to intra- and inter-operator variability. There is an untapped amount of complementary information from both bright- and black-blood images that offers solutions to these challenges, and that was not exploited until now.

The present study introduces an innovative CMR technology, SPOT, that simultaneously acquires both bright- and black-blood images, offering high sensitivity for detecting and localizing myocardial injuries. This technology is ideally suited for AI-powered automated scar quantification.

The key findings of this study include:

(1) Enhanced scar detection and localization: joint bright- and black-blood SPOT imaging allows for enhanced scar-blood-healthy-myocardium contrast, supporting more sensitive scar detection and localization.
(2) Improved reproducibility of LV wall segmentation: LV wall segmentation is more reproducible on SPOT than conventional bright-blood LGE imaging, paving the way for its automation.
(3) AI-powered quantification: leveraging AI-powered tools enables robust and fully automated quantification of myocardial scars.

SPOT imaging

Several groups have introduced black-blood or dark-/gray-blood imaging techniques, which effectively reveal scar patterns obscured by blood signal. Gray-blood LGE methods—often achieved via partial blood signal suppression—have shown promise in improving subendocardial scar detection and offer the benefit of easy integration into clinical protocols[12,17,18]. However, their contrast remains suboptimal, and the incomplete suppression of the blood signal can still lead to ambiguity at the blood-myocardium interface. Additionally, these techniques may not sufficiently suppress myocardial signal to highlight scar conspicuity in all contexts. Black-blood approaches achieve more complete suppression of both blood and healthy myocardium signals, offering improved scar contrast, but they compromise anatomical detail, making it difficult to assess scar location and transmurality with confidence. SPOT overcomes these trade-offs by simultaneously acquiring co-registered bright- and black-blood images, thereby allowing the independent optimization of scar visualization and anatomical delineation. This synergy is key to enabling both accurate visual interpretation and robust, automated scar quantification. While the current SPOT implementation uses a single-shot

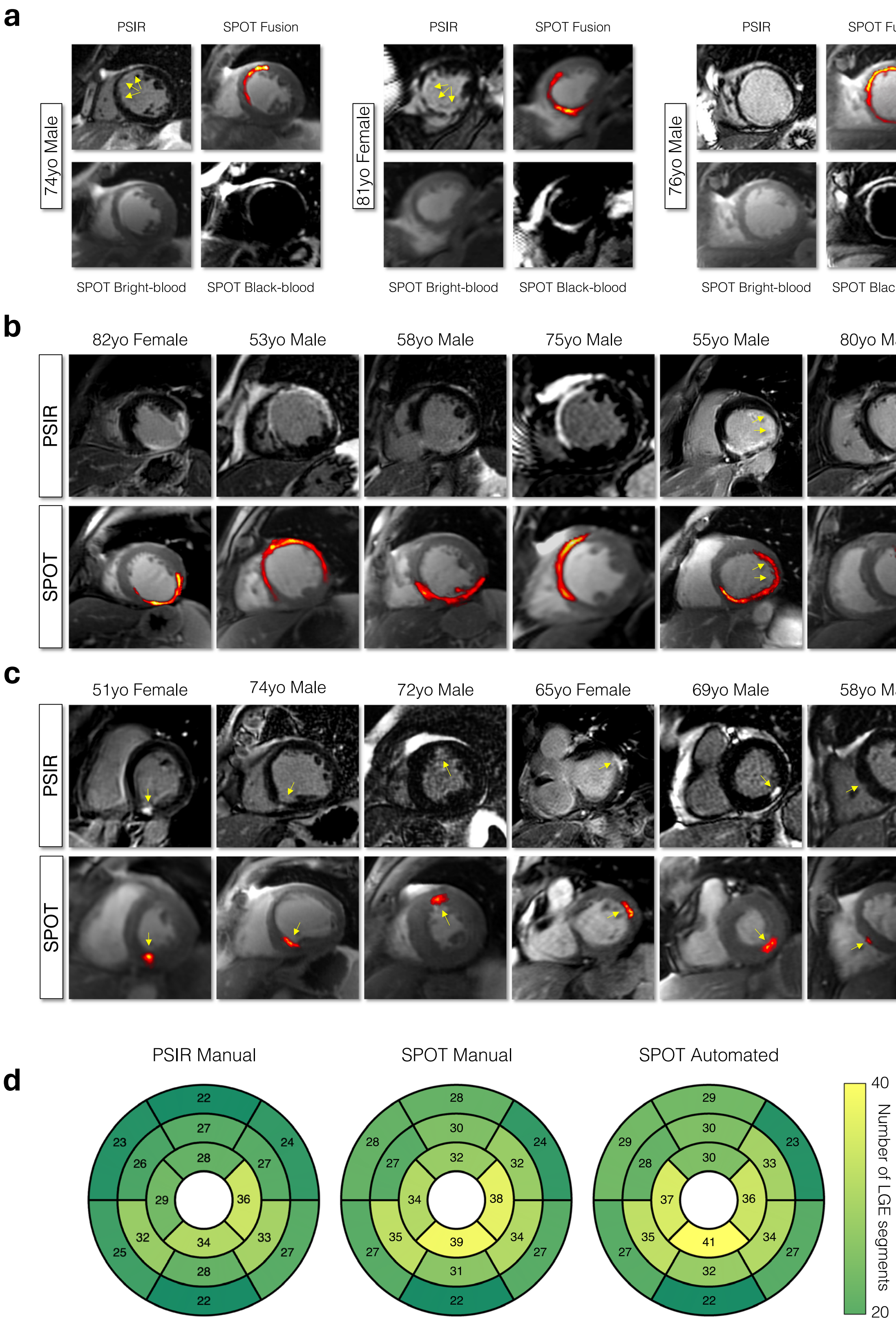

readout to maintain consistency with the reference 2D PSIR protocol and to ensure robustness in patients with arrhythmia or limited breath-holding capacity, the use of a segmented-readout 3D SPOT version holds promise for achieving higher spatial resolution. This direction will be explored in future studies to further enhance anatomical detail.

Visual and quantitative consistency

In animal models, SPOT imaging showed remarkable visual consistency with histopathologic images in terms of geographical distribution, size, and extent of the lesions. Clear collagen accumulation was evident on Masson trichrome histology at the injury and ablations sites.

Fig. 6 | Illustrative SPOT images collected in patients and distribution of LGE segments. a Illustrative examples of SPOT images collected from three patients with myocardial infarction, demonstrating the challenges in accurately delineating subendocardial and scar contours using reference phase-sensitive inversion recovery (PSIR) imaging. Yellow arrows indicate scar areas that are difficult to delineate on PSIR images. **b** Illustrative PSIR and SPOT images from the testing set collected on six patients with large myocardial scars. Yellow arrows highlight scar areas that are difficult to delineate on PSIR images, often due to poor contrast or ambiguous boundaries. SPOT imaging clearly delineates these scar regions. **c** PSIR and SPOT images from six patients with small, localized myocardial scars. Yellow arrows indicate scar locations, which are difficult to detect on PSIR images due to their subtlety and proximity to the blood pool. **d** Distribution of LGE segments across the entire testing set, represented in American Heart Association (AHA) bullseye plots. The regional distribution of LGE segments is shown for reference PSIR imaging, alongside comparisons with manual and fully automated SPOT analyses. The plots illustrate the superior detection and localization of LGE segments using SPOT imaging, both with manual and automated assessments.

In patients, the EPG-guided SPOT technology offers immediate and color-coded images, enhancing diagnostic capabilities. Our findings demonstrate the superior sensitivity of SPOT in detecting myocardial injuries compared with conventional bright-blood PSIR method. Specifically, there was an 11.2% increase in the detection of LGE segments on SPOT compared with conventional PSIR (419/800 vs. 466/800 segments, $P < 0.05$). This observation aligns well with prior research reporting the enhanced sensitivity of black-blood imaging techniques. For instance, Sridi et al. reported an additional 16% of hyperenhanced segments[16], while Francis R et al. observed a 41.5% increase in LGE segments[19]. These findings underscore that the increased sensitivity is directly attributable to the effective and simultaneous cancellation of blood and healthy myocardium signals.

Reproducibility and automation

The segmentation of LV wall contours on bright-blood PSIR LGE images, whether performed manually or through automation, has long been hindered by the lack of contrast between blood and scar regions. Consequently, considerable research efforts have been directed towards leveraging LV contours obtained from alternative CMR sequences, such as CINE, as prior knowledge[20,21]. However, these approaches introduce several challenges, including the need to address rigid and nonrigid multi-contrast deformations arising from differences in breath-holding positions between CINE and LGE images, patient motion as well as discrepancies in acquisition parameters, such as spatial resolution and field-of-view.

To circumvent these complexities, our technology offers a unique solution by providing co-registered bright-blood images (depicting heart anatomy) and black-blood images (highlighting scar tissue) acquired under identical breath-holding and acquisition parameters. This feature renders our approach ideally suited for automated LV wall segmentation and facilitates seamless propagation onto black-blood scar images, eliminating the aforementioned challenges associated with integrating data from disparate CMR sequences.

Automated segmentation of LV wall showed excellent agreement with manual processing, with a DICE coefficient of 78.5% [IQR 76.4–81.2], a result consistent with previously reported values from CINE images[22,23]. The DICE index for LV wall segmentation was higher in SPOT images compared to PSIR images, albeit with lower values noted for apical slices, likely attributable to partial volume effects. We employed a state-of-the-art transformer model for slice-by-slice segmentation. We anticipate further improvements by harnessing the 3D anatomical structure information inherent to the multi-slice data, as input for a network using an ensemble of modified 2D and 3D models[24]. This will be explored in the future.

Scar segmentation–algorithm choice and performance

With blood and healthy myocardium signals being completely suppressed and scar signal predominantly bright on black-blood SPOT images, robust automated scar segmentation and quantification become reachable with straightforward image processing algorithms. Several established techniques, including seeded region growing, n-SD, and FWHM, were evaluated against ground truth manual segmentations. It is noteworthy that n-SD and FWHM require a region of remote and scarred myocardium, and their outcomes may vary depending on the position and size of these regions as well as differences among operators. The automated region growing technique, using a distance ε of 0.15, outperformed other methods, eliminating the need for operator intervention.

Comparison with manual segmentation

The proposed segmentation method surpassed DICE scores reported in previous studies for LV scar quantification, with a median middle slice DICE of 89.4%. This represents a notable improvement compared to existing literature where Kurzendorfer et al.[25] reported a mean DICE of 66%, Popescu et al.[26] achieved a mean DICE of 57%, and Tao et al.[27] achieved a mean DICE of 83%. SPOT imaging not only enhanced expert confidence but also reduced discrepancies among experts in scar volume, extent, and transmurality when compared to standard LGE techniques. Excellent agreement was observed between manual and automated SPOT segmentation for scar volume, extent, and transmurality, with ICCs exceeding 0.95 ($P > 0.05$), suggesting that this framework is reliable for accurate myocardial scar assessment in clinical settings. Additionally, AI-based segmentation offered near real-time processing (5 s versus 20 min), reducing clinician workload and minimizing interobserver variability.

Clinical implications

SPOT holds significant clinical implications. Firstly, its capacity for more reproducible interpretation of myocardial scars with CMR, requiring less expertise, addresses a longstanding challenge in LGE image interpretation, known for its long learning curve. SPOT's ability to detect concealed myocardial injuries is particularly valuable for diagnosis structural heart disease or identifying the cause of acute coronary syndromes with non-obstructed coronary arteries, a scenario where uncertainty persist in up to 30% of cases. This uncertainty often stems from intra-pixel abnormalities or small lesions undetected due to blood pool proximity[28], a common occurrence as illustrated by the clinical scenario of the 58-year-old male in Fig. 6c.

Moreover, SPOT enables a more thorough and robust assessment of scar size and extent beyond arbitrary endocardial segmentation. This may significantly impact the primary prevention of sudden cardiac death by better predicting ventricular arrhythmia events across ischemic, dilated, and hypertrophic cardiomyopathies. Although scar quantification has shown potential to better select candidates for defibrillators[29], the recommended strategy in ischemic heart disease remains based on ejection fraction measurements as scar quantification on bright-blood LGE images still lacks robustness[30].

Recent observations also suggest that further enhancements in contrast and/or spatial resolution, facilitated by SPOT, could unveil occult structural defects beyond the reach of current CMR techniques, offering substantial benefits in ventricular arrhythmia management. Indeed, invasive catheter mapping data acquired in survivors of sudden cardiac death has revealed that up to two-thirds of patients with apparently normal hearts on CMR do have concealed electrical conduction abnormalities[31], suggesting occult structural defects undetected using the bright-blood LGE technique.

Finally, SPOT's integration into scar quantification and modeling approaches for intraprocedural guidance or risk stratification purposes addresses the labor-intensive nature and reliance on local expertise, thus making these strategies more scalable for broader clinical use. The minimal impact on CMR study duration, with SPOT adding less than 5 min, renders its adoption both feasible and highly practical.

Study limitations

The study presents several limitations. On the sequence side, the reliance on breath-holding during data acquisition introduces susceptibility to motion artifacts, particularly problematic in protocols necessitating repetitive breath-holds and unsuitable for patients with severe dyspnea. While only a minimal proportion of patients in our recruited cohort (6.7%) exhibited residual artifacts, the implementation of a free-breathing version of the sequence, as proposed by Sridi et al.[16], could alleviate these challenges. Furthermore, the limitation of 2D acquisitions may lead to potential lesion underestimation due to restricted coverage, sampling error, and partial volume averaging. The implementation of a 3D free-breathing version of SPOT[32] would offer enhanced coverage, particularly beneficial for ablation-guided therapy and the assessment of scars in thinner tissues, such as the right ventricle and the left atrium.

While the proposed SPOT sequence was developed and validated at 1.5-T, its translation to 3.0-T systems—a common setting in many clinical centers—requires several technical adaptations. At 3.0-T, the increased susceptibility to bSSFP-related artifacts necessitates switching to a gradient echo read-out to mitigate dark banding and blood-flow artifacts. Additionally, specific absorption rate constraints at higher field strengths may require the implementation of a fully adiabatic T1-rho preparation module. Moreover, the automated segmentation and landmark detection algorithms–currently trained on 1.5-T datasets–may require retraining on dedicated 3.0-T datasets to maintain performance consistency. While the readout and preparation modules have already been adapted for 3.0-T in preliminary work, broader deployment will depend on the acquisition of sufficiently large and diverse imaging 3.0-T imaging datasets for algorithm retraining and validation.

Moreover, while SPOT currently employs fat suppression only for bright-blood imaging, the delineation of intramyocardial fat remains an important unmet need, especially given its potential arrhythmogenic role in ischemic and nonischemic cardiomyopathies. Incorporating fat-sensitive techniques into SPOT, such as a Dixon-based approach, could offer a promising strategy for visualizing fibrofatty infiltration[33,34]. Though this would require adjustments to both acquisition and processing pipelines, it represents a compelling direction for expanding SPOT's tissue characterization capabilities.

On the processing side, the LV wall segmentation network could benefit from a larger and more diverse cohort encompassing various data from different centers, systems, and scar patterns associated with different cardiomyopathies. Additionally, as a supervised network, our algorithm's performance is directly influenced by the quality of the ground truth data used during training, thus establishing an inherent limit on its potential performance. We also acknowledge that the testing dataset contained a higher proportion of LCx-related infarctions compared to the training dataset. Although this imbalance reflected random selection from a real-world cohort and did not adversely affect SPOT's performance in this subgroup, future studies will incorporate stratified sampling and additional multicenter data to ensure anatomical balance across coronary territories. Moreover, integration of quality control measures is imperative to mitigate motion-related artifacts, image blurring due to arrhythmias, mistriggering, or residual motion, all of which could compromise image quality and diagnostic accuracy in clinical practice. Robust and fully automated quality control mechanisms are crucial for clinical translation and will be explored in future studies. Finally, although the study's single-center, single-vendor, and single magnetic field strength design may introduce center-specific biases, the use of an open-source Gadgetron-based post-processing implementation paves the way for seamless integration across multiple vendors in the future.

On the clinical side, the exclusive focus of the study on ischemic patients may limit the algorithm's applicability to nonischemic cardiomyopathies. Additional research is needed to broaden the application of the proposed framework to the full spectrum of cardiomyopathies. Finally, multicenter and multivendor validation studies that correlate the proposed framework with clinical outcomes across broader range of pathologies will inform the subsequent steps toward widespread clinical use.

In conclusion, the proposed AI-powered SPOT imaging pipeline represents a significant advancement in imaging patients with heart disease. It delivers images with unprecedented scar contrast embedded in a detailed heart anatomy, along with a fast, robust, fully automated, and cost-effective quantification of myocardial scar. In doing so, this innovation may provide opportunities for earlier detection and improved therapeutic management of ischemic heart disease, transforming clinical practices and patient outcomes.

Methods

Sequence design: joint bright- and black-blood LGE imaging (SPOT)

Sequence details. We propose a 2D imaging technology, termed SPOT (scar-specific imaging with Preserved myOcardial visualizaTion), which simultaneously acquires "black-blood" and "bright-blood" LGE images in an interleaved fashion (Fig. 1). The black-blood image eliminates signals from both healthy myocardium and blood, optimizing scar detection, while the bright-blood image preserved blood-myocardium contrast, enhancing scar localization (Fig. 1). SPOT is a single-shot electrocardiogram-triggered 2D balanced steady-state free-precession sequence that alternates between these two contrasts on consecutive heartbeats: in odd heartbeats, a 180° nonselective inversion pulse (pulse duration = 10 msec) is followed by a T1-rho module[35] (pulse duration = 27 msec) to generate black-blood contrast. In even heartbeats, only a T1-rho module is played out to generate bright-blood contrast. The inclusion of this module in bright-blood acquisition is essential to enhance contrast between the blood pool and myocardium, thereby facilitating accurate segmentation of the LV wall. The T1-rho module includes an initial 90° tip-down pulse along the x-axis to rotate the magnetization, followed by four spin-lock pulses with alternating phases ($SL_{\pm y}$) and fixed duration, and by two adiabatic refocusing pulses ($180_{\pm y}$). A final 90° tip-up pulsed is then used to return the magnetization to the z-axis. The rotation angle of the spin-lock components was defined as $\alpha_{SL} = 2\pi \times FSL \times TSL$, where FSL and TSL are the spin-lock frequency and spin-lock time, respectively. A crusher gradient is then used to remove any residual transverse magnetization. For each slice, eight single-shot images (four bright-blood and four black-blood images) were acquired in mid-diastole over 10 heartbeats, with the first two heartbeats serving as dummy cycles. Data were acquired over multiple breath-holds with full ventricular coverage. Detailed imaging parameters are provided in Supplementary Fig. 11, including 10–20 slices, 4 signal averages, 1.5 × 1.5 mm in-plane resolution, 8 mm slice thickness, FSL = 500 Hz, TSL = 27 msec, flip angle = 60°, GRAPPA ×2 (36 calibration lines), ~160 msec acquisition window, echo time = 1.2 msec, repetition time = 2.8 msec, bandwidth = 849 Hz/pixel. The inversion time (TI) was determined from a prior scout acquisition.

Image reconstruction details. Single-shot images are reconstructed with a parallel imaging GRAPPA algorithm[36] followed by image averaging to restore signal-to-noise. Each single-shot image is reconstructed on-the-fly at the scanner and displayed in real-time for rapid assessment of image contrast. Imaging parameters, including the field of view (FOV) and slices positions, are adjusted as necessary, and the scan can be restarted if required. A colored-fusion of the reconstructed bright- and black-blood images is also provided for optimal detection and localization of myocardial injuries. Upon completing the acquisition of the short-axis stack of slices, the entire reconstruction process, including image averaging, is completed in under 10 s.

Fully automated black-blood contrast selection (TI-scout). A dedicated free-breathing SPOT scout sequence was employed prior to the whole-heart acquisition to determine the TI that achieves optimal suppression of both healthy myocardium and blood signals. This sequence acquired 14 mid-ventricular black-blood images with increasing TIs (ranging from 60 to 190 msec with a 10 msec increment) in the odd heartbeats and 14 bright-blood images in the even heartbeats, over a total scan time of 28 heartbeats. A fully automated algorithm, detailed in de Villedon de Naide et al.[37,38], automatically selected the optimal TI by identifying from the scout images the image with the darkest blood and healthy myocardium signals. The algorithm is available on GitHub (https://github.com/smheart/autoTI/).

Image processing

Automated transformer-based LV segmentation. A state-of-the-art transformer-based model for medical image segmentation, inspired by Dosovitskiy et al.[39], was employed. The architecture, detailed in Gao et al.[40], is based on a hybrid approach to semantic segmentation, leveraging both the power of convolutional filters, and their ability to extract local features, with the advantages of vision transformers, with attention maps, which help the network to be less dependent on local space features. Images are first divided into patches, and these patches are embedded using a convolutional encoder. Each downsampling block then downsamples and processes the embedding using a bi-directional transformer block, and each upsampling block does the same operations, in an upsampling manner. At every scale, semantic maps derived from the bi-directional multi-head attention block in the bi-directional transformer block are extracted and then used together using a multi-scale fusion process and skip connections to maintain high-level information that could have been lost during the downsampling phase. The final embeddings are then decoded using a convolutional decoder to output the segmentation map. This architecture is highly data efficient and delivers state-of-the-art performance on medical datasets, particularly in scenarios with limited training data[41]. The settings were essentially replicated from Gao et al.[40].

Right ventricular insertion points detection and AHA's 16-segment model creation. Accurate detection of right ventricular insertion points is crucial for constructing the 16-segment AHA bullseye model. A conventional U-net-based method[42,43] was employed to automatically detect anterior and posterior right ventricular insertion points within short-axis bright-blood images. The SoftMax activation function was used to generate confidence scores, representing the probability of accurate landmark detection. Confidence calibration assesses the model's ability to provide precise correctness probabilities for predictions. To define segments within a cardiac level, both anterior and posterior right ventricular insertion points were used to establish two major axes[44,45]. For the basal and mid-cavity levels, the septal and lateral areas were further divided into six segments using an equiangular line. Finally, a 16-segment AHA bullseye model was created by incorporating both landmarks and LV contours.

Implementation details, pre-processing, and labels. The training dataset consisted of 400 patients (62.3 ± 11.7 years, 22% female, 5052 2D images) with known or suspected ischemic heart disease. This dataset was split into a training (85%) and a validation (15%) set used for U-net-based landmark detection and Transformer-based LV segmentation. There was no overlap between the testing dataset and the training/validation data, ensuring the independence of test data.

Manual delineation of the endocardial and epicardial contours and identification of right ventricular insertion points were carried out by three expert annotators. Care was taken to exclude the papillary muscles from the segmentation. The annotations were performed using CVI42 (Circle Cardiovascular Imaging, Calgary, Canada) and were exported as an.xml file for further processing in Python.

Training was conducted on a dedicated workstation with Intel Xeon Gold 6154, 3 GHz, 18 cores, 36 threads, NVIDIA Tesla V100 32 Go GPU, 377 GB RAM, Python version 2.7.18, Ubuntu Linux 18.04.6 LTS, CUDA 11.6, and TensorFlow 2.8.0.

Data augmentation was used to avoid overfitting and included random rotations, flips, contrast adjustment, sharpness adjustment and Rician noise addition. The following parameters were used: equally weighted binary cross-entropy and dice loss, learning rate 10^{-3}, cropped 240 × 240 mm bright-blood image as input, binary LV wall as output, normalization to zero mean and standard deviation of one. The model was trained using the AdamW optimizer for 77 epochs with a batch size of 8 and weight decay of 0.01. For the insertion points detection model, the same hyperparameters as previously defined were employed, with the exception of the pixel-wise Euclidean distance loss and a base learning rate of 10^{-4}. The training took approximately 2 h.

Myocardial scar quantification

Myocardial scar thresholding. A fast and robust seeded region-growing algorithm was used to automatically segment scar tissue on black-blood SPOT images[46]. The segmentation process initiates from a seed point, and the neighboring pixels to this point are assessed to determine their inclusion in the object. The disparity between a pixel's intensity value and the mean intensity of the region serves as a measure of similarity. The maximum distance ε was optimized for our application (see below). The pixel with the smallest disparity, measured in this manner, is assigned to the respective region. This process continues until all pixels within the LV wall are allocated to a region. This approach necessitates only a seed point as input, which was automatically selected as the LV center of mass. Prior to scar segmentation, the distribution of pixels within the LV wall was adjusted using a standard histogram-based intensity scaling.

Myocardial scar quantification: presence, volume, extent, and transmurality. Scar size was quantified in both volume (mL) and extent (percentage of total myocardial volume). Scar transmurality was assessed using the established centerline chord method[47,48], which segments each myocardial slice into 100 evenly distributed chords and calculates infarct extent along the length of each chord. Average transmurality was determined by considering only chords where the infarct extent was at least 1%.

Clinical integration and display

To assess the practical utility of the proposed framework in a clinical hospital environment, an inline point-of-care implementation of the pipeline was seamlessly integrated onto a clinical 1.5-T MRI scanner (MAGNETOM Aera, Siemens Healthcare, Erlangen, Germany, VE11C software version) using the Gadgetron framework (v4.1.1)[49]. Model inference was conducted on a workstation equipped with an Intel Xeon CPU E5-2698 v4, 2.20 GHz, with 20 cores, 40 threads, NVIDIA Tesla K80 GPU, 512 GB RAM, Python 2.7.18, Ubuntu Linux 20.04.6, CUDA 11.4, TensorFlow 2.9.1. Reconstructed images were transmitted back to the user interface, featuring a color-fusion of bright- and black-blood images. These images were enriched with overlaid LV contours, AHA 16-segment bullseyes indicating scar size and scar transmurality, right ventricular insertion points, and associated confidence scores. A comprehensive report including LV volume, total scar volume, scar burden, and scar transmurality was generated automatically. The entire process required no user interaction.

The codes employed for training the segmentation and landmark models, the pre-trained models, and the Gadgetron gadgets are readily available at: https://github.com/smheart/SPOT.

Validation with extended graph simulations

EPG simulations[50] were conducted to analyze the signal evolution of the proposed SPOT sequence as a function of time and define optimal parameter ranges for in vivo studies. The sequence was simulated for T1/T2 characteristics of post-contrast blood (460/140 msec), viable myocardium (670/42 msec) and scar (440/44 msec) at 1.5-T, and for a heart rate of 60 beats per minute. The influences of the timing parameters TI (ranging from 1 to 300 msec) and T1-rho preparation times (ranging from 1 to 200 msec) were examined for their effectiveness in suppressing both blood and myocardium signals (SPOT black-blood image, scar detection) and in providing sufficient myocardium-blood contrast (SPOT bright-blood image, anatomical assessment). Simulations were performed in MATLAB (version R2023b Update 5, The MathWorks, Natick, MA, USA).

Validation in a phantom setting

A static phantom experiment was performed to assess the bright- and black-blood properties of the proposed SPOT sequence. The T1MES phantom, which comprises 9 vials with known T1 and T2 values characteristics of post-contrast blood, scar, and healthy myocardium, was used[51].

Phantom imaging. Imaging parameters for the phantom study included a FOV of 270 mm^2 and simulated electrocardiogram of 60 beats per minute. Other relevant scan parameters are shown in Supplementary Fig. 11. Two different acquisitions were performed for comparison purposes: (i) a SPOT acquisition as described above, and (ii) a conventional bright-blood PSIR acquisition. The TI was set to null the signal from the vial mimicking viable myocardium for the reference PSIR sequence and to null the signal from the vials simulating blood and myocardium tissues for the SPOT sequence.

Phantom data analysis. All images were analyzed by drawing circular regions-of-interest with an aera of 1.9 cm^2 in the phantom vials mimicking post-contrast blood, myocardium, and scar tissues. Mean signal intensities were extracted for each vial and compared for both SPOT and PSIR acquisitions to assess the effectiveness of the SPOT sequence in distinguishing between these tissue types.

Validation in animal models

The optimized SPOT sequence was further validated in large animal models to assess its capability to accurately characterize scar tissue using gold standard histology and gross pathology. The study adhered to the EU Directive 2010/63/EU on the ethical treatment of animals used for scientific research. Approval was obtained from the ethical committee (CEEA50) of the French Ministry for Research and Innovation (approval number 7995). All animal experimentations were conducted at IHU LIRYC, Bordeaux, France, following the requisite regulatory approvals.

Animal care and preparation for imaging. Sheep were housed in appropriate facilities at IHU LIRYC with controlled temperature and humidity. Animals were provided a standard diet until the day preceding interventions, when they were fasted to minimize anesthesia-related risks. On the day of the procedure, animals were transferred on a dedicated trolley to the operating table and prepared under general anesthesia. General anesthesia included pre-, intra-, and post-operative analgesia with anti-inflammatory and analgesic medication, specifically Sufentanil at a dosage of 0.15 μg/kg/h. To facilitate heart rate monitoring and synchronize data acquisition during imaging, MR-compatible leads were attached to the animal. Additionally, a peripheral catheter was inserted into the internal jugular vein for drug infusion purposes. Anesthesia induction involved the administration of Propofol at a dosage of 1–2 mg/kg, followed by maintenance with isoflurane ranging from 1.5 to 3%, supplemented with a continuous infusion of midazolam at 0.5 mg/kg via endotracheal intubation. Mechanical ventilation, utilizing Aestiva/5 equipment (Datex Ohmeda, GE Healthcare, Waukesha, Wis, USA) was employed to regulate breathing rates. Methods to reduce pain, suffering, and anxiety were applied throughout the procedure. Continuous monitoring ensured the maintenance of physiological parameters within normal ranges, including heart rate, arterial pressure, body temperature, oxygen saturation, and CO2 levels. Intravenous infusion of amiodarone at 1 mg/kg/h was employed to prevent arrhythmias.

Animal models of myocardial infarction. Two chronic models of myocardial infarction were developed in two female sheep by an experienced interventional cardiologist (P.J.) to mimic human infarction:

(i) a model of heterogenous post-infarction scar induced by temporary balloon occlusion (ischemia-reperfusion method) in the left anterior descending artery in a 2-year-old sheep[52]. Reperfusion is then performed under anti-arrhythmic medication after 90 min to obtain sufficient salvaged myocardium.

(ii) A model of micro-infarction induced by multifocal endocardial ablation with radiofrequency catheters (Biosense Webster, Diamond Bar, CA) in a 3-year-old sheep. Multiple distinct focal lesions were created in the electrophysiology laboratory.

Upon awakening, the animals were closely monitored until fully awake. Monitoring included assessment of posture, mobility, and signs of pain. Analgesics were administered if necessary. At the laboratory, the animal is returned to its initial housing conditions with species-appropriate refinements: social group, salt block, hay, and straw bedding. Animals are monitored daily by animal care personnel. Animals were then returned to the care of their attendants for the development of chronic healed scar. Subsequently, at the three-month mark, the animals returned to the laboratory for imaging procedures prior to undergoing ex vivo characterization.

Imaging data acquisition. All CMR images were collected in mid-diastole at end-expiration with the ventilator suspended at the time of breath-hold. A 32-channel spin coil and a dedicated 18-channel body coil were used. Post-contrast whole-heart PSIR and SPOT short-axis images were acquired in random order 15 min after the intravenous injection of 0.2 mmol/kg gadoterate meglumine (Dotarem®, Guerbet). Detailed imaging parameters are provided in Supplementary Fig. 11.

Histological data acquisition. Following imaging, animals were euthanized under general anesthesia by inducing ventricular fibrillation, followed by cardiac arrest using a cardioplegic solution (Celsior®, Genzyme Corp, Boston, MA) to preserve organ integrity and prevent interference with histological outcomes. Hearts were carefully dissected, and tissue specimens were fixed in paraformaldehyde (4%) to maintain structural integrity.

Automated dehydration was performed using a Leica HistoCore Pearl processor (Wetzlar, Germany) before embedding the specimens in paraffin. Short-axis slices of 6 μm thickness were prepared using a microtome and stained with Masson's trichrome to highlight myocytes (red), collagen (green), and nuclei (black). Sections were digitally scanned at 20x magnification, and histological image analysis and sectioning were performed using Zen Blue software (Zeiss, Oberkochen, Germany).

Animal data analysis. The SPOT images were visually inspected to evaluate their overall quality and efficacy in attenuating blood and healthy myocardium signals. Each image was scrutinized to discern regions depicting both injured and healthy myocardium. Subsequently, a comparative analysis was conducted to ascertain spatial congruence of injuries among CMR images, histological findings (blue representing fibrosis, red depicting myocardial fibers), and gross pathology.

Pipeline validation in cardiac patients

Population and study design. From March 2021 to June 2023, 516 patients undergoing CMR in our institution were prospectively included. The inclusion criterion was a clinical indication to undergo contrast-enhanced CMR for known or suspected ischemic heart disease. Noninclusion criteria included age <18 years old, history of allergic reaction to gadolinium-based contrast agents, history of severe renal failure, presence of a non-MR-conditional implantable device, inability to lay on the back for 50 min, pregnancy, breast-feeding, and inability to express informed consent. Patients were not consecutive as the inclusion depended on the clinical workflow and was also impacted by competing research projects on similar patients. The study followed the STROBE reporting guidelines, was approved by the Biomedical Research Ethics Committee (approvals 2016-A01578-43 and 2023-A00872-43), and all patients provided written informed consent for participation in this study.

Cardiac magnetic resonance protocol. All patients underwent CMR in the supine position using a 1.5-T clinical system (MAGNETOM Aera, Siemens Healthcare, Erlangen, Germany), equipped with a dedicated 32-channel spine coil and an 18-channel body coil. The CMR protocol comprised standard cine imaging, capturing two-, three-, and four-chamber views, along with a stack of contiguous short-axis slices encompassing the ventricles. LGE imaging was conducted 12 min post-administration of 0.2 mmol/kg gadoteric meglumine (Dotarem, Guerbet, France) using both the proposed SPOT sequence and a breath-held PSIR sequence in a short-axis stack of contiguous slices covering the ventricles. TIs were meticulously adjusted to null viable myocardium for PSIR imaging. Parameters for the LGE sequences are detailed in Supplementary Fig. 11.

Imaging data processing. The dataset from the final study cohort was randomly divided into a training set (400 patients, 5755 2D images) and a testing set (50 patients, 703 2D images). Within the testing set, two experienced cardiac radiologists (S.S. and J.M., with 8 and 5 years of CMR experience, respectively), meticulously delineated endocardial and epicardial borders, hyperenhanced scar regions, along with right ventricular insertion points using CVI42 (Circle Cardiovascular Imaging, Calgary, Canada). Image analysis was performed across both PSIR and SPOT images, adhering to the recent 2020 recommendations from the Society for Cardiovascular Magnetic Resonance[53]. Care was taken to excluding trabecular tissue and papillary muscles from myocardial segmentation. Both observers were blinded to the output of the algorithms and were unaware of the labels provided by their counterpart. One of the experts (J.M.) conducted an independent re-annotation of the entire testing cohort during a second session, held over a month following the initial annotation process. Manual segmentation, along with the resulting clinical measures, served as the gold standard for comparison. Processing and acquisition times were recorded for all scans, taking into account pauses occurring between breath-holds.

Performance evaluation. The accuracy of myocardial wall and scar segmentations was evaluated using the DICE score (0% denoting no overlap, and 100% denoting perfect agreement)[54]. Assessments included both intra- and interobserver variability, comparison of automated versus manual segmentation, and analysis across different slice positions (apical, middle, basal, and all slices).

The accuracy of detected right ventricular insertion points was assessed using the model's confidence scores (ranging from 0 for poor accuracy to 1 for excellent accuracy, as a continuous variable), Euclidean distances, and angular measurements (in degrees) relative to the LV center of mass as the reference point. This evaluation was conducted in comparison to manually identified reference points for both A-RVI and P-RVI.

Image quality was assessed for SPOT and PSIR images, focusing on susceptibility, motion, and blood flow artifacts, and suboptimal image contrast. To evaluate the efficacy of the SPOT in mitigating both blood and myocardial signals, signal intensities in patients were quantified and compared for scar, myocardium, and blood tissues. This analysis involved reference PSIR, SPOT black-blood, and SPOT bright-blood images.

Scar quantification involved comparing different semi-automated methods using SPOT images, including FWHM, n-SD (n ranging from 1 to 4), and region growing with varying distance factors (ε from 0.03 to 0.27). The FWHM method defines scar region as areas where the signal intensity exceeds 50% of the maximum signal intensity within manually labeled scar regions. For the n-SD techniques, scar regions were identified as aeras exhibiting signal intensities surpassing n standard deviations from the mean of the remote (non-infarcted) myocardium region of interest, which was defined manually.

Intra- and interobserver reproducibility were evaluated for scar volume, extent, and transmurality measurements using SPOT and PSIR images. Additionally, scar quantification involved comparisons between manual and automated SPOT techniques, manual SPOT versus PSIR, and automated SPOT versus PSIR, assessing scar volume (in mL), extent (in % of LV mass), and transmurality (in %). Finally, the number of patients with LGE and the number of AHA segments exhibiting LGE were reported for both sequences.

Statistical analysis

Statistical analysis was performed using SPSS Statistics v28 (IBM Corp., Armonk, NY). Descriptive statistics were employed. The Shapiro–Wilk test was used to test the null hypothesis that each continuous variable follows a normal distribution. Continuous variables are presented as mean ± standard deviation when following a normal distribution and as median [interquartile range Q1–Q3] otherwise. Categorical variables are presented as fraction (%). Dependent continuous variables were compared using paired-sample parametric (paired Student's t test) or nonparametric (Wilcoxon signed rank test) tests depending on data normality. Independent continuous variables were compared using independent-sample parametric (unpaired Student's t test) or non-parametric (Mann–Whitney U test) tests depending on data normality. Categorical variables were compared using χ^2. Statistical analysis of intra- and interobserver-variability was performed using ICC with 95% CI. Agreement was considered poor, moderate, good, or excellent for ICC < 0.50, 0.50–0.75, 0.75–0.90, and >0.90, respectively. Cohen's kappa statistics were employed to evaluate agreement between techniques and observers, with the level of agreement defined as poor ($\kappa < 0.21$), fair ($\kappa = 0.21–0.40$), moderate ($\kappa = 0.41–0.60$), substantial ($\kappa = 0.61–0.80$), and almost perfect ($\kappa > 0.80$). Bland-Altman analysis was conducted to evaluate agreement between measurement methods and observers, reporting both the mean difference (bias) and the standard deviation of differences (variability), which together reflect systematic error and reproducibility limits. A $P < 0.05$ was considered to indicate statistical significance.

Reporting summary

Further information on research design is available in the Nature Portfolio Reporting Summary linked to this article.

Data availability

Simulation and phantom datasets are available at https://github.com/smheart/SPOT/ and on Zenodo (https://doi.org/10.5281/zenodo.17183014). The SPOT sequence will be made available for sharing in *syngo* MR VE11C on the Siemens' C2P platform. The exar1 protocols for the 1.5-T MAGNETOM Aera and the MAGNETOM Avanto (software version *syngo* MR VE11C) will be available to download at: magnetomworld.siemens-healthineers.com/clinical-corner/protocols > Cardiovascular MRI. Source data are provided with this paper.

Code availability

EPG simulation, automated LV segmentation, and scar processing codes as well as trained networks can be accessed at https://github.com/smheart/SPOT/ and on Zenodo (https://doi.org/10.5281/zenodo.17183014). The code for fully automated processing of TI-scout images can be accessed at https://github.com/smheart/autoTI/ and on Zenodo (https://doi.org/10.5281/zenodo.17182725).

References

1. Kim, R. J. et al. Relationship of MRI delayed contrast enhancement to irreversible injury, infarct age, and contractile function. *Circulation* **100**, 1992–2002 (1999).
2. Pegg, T. J. et al. Prediction of global left ventricular functional recovery in patients with heart failure undergoing surgical revascularisation, based on late gadolinium enhancement cardiovascular magnetic resonance. *J. Cardiovasc. Magn. Reson.* **12**, 1–10 (2010).
3. Kim, R. J. et al. The use of contrast-enhanced magnetic resonance imaging to identify reversible myocardial dysfunction. *N. Engl. J. Med* **343**, 1445–1453 (2000).
4. Alexandre, J. et al. Scar extent evaluated by late gadolinium enhancement CMR: A powerful predictor of long term appropriate ICD therapy in patients with coronary artery disease. *J. Cardiovasc. Magn. Reson.* **15**, 1–11 (2013).
5. Scott, P. A. et al. The extent of left ventricular scar quantified by late gadolinium enhancement MRI is associated with spontaneous ventricular arrhythmias in patients with coronary artery disease and implantable cardioverter-defibrillators. *Circ. Arrhythm. Electrophysiol.* **4**, 324–330 (2011).
6. Vergara, G. R. & Marrouche, N. F. Tailored management of atrial fibrillation using a LGE-MRI based model: from the clinic to the electrophysiology laboratory. *J. Cardiovasc. Electrophysiol.* **22**, 481–487 (2011).
7. Yamashita, S. et al. Image integration to guide catheter ablation in scar-related ventricular tachycardia. *J. Cardiovasc. Electrophysiol.* **27**, 699–708 (2016).
8. Farrelly, C. et al. Improved detection of subendocardial hyperenhancement in myocardial infarction using dark blood-pool delayed enhancement MRI. *Am. J. Roentgenol.* **196**, 339–348 (2011).
9. Flett, A. S. et al. Evaluation of techniques for the quantification of myocardial scar of differing etiology using cardiac magnetic resonance. *JACC Cardiovasc. Imaging* **4**, 150–156 (2011).
10. Mewton, N., Revel, D., Bonnefoy, E., Ovize, M. & Croisille, P. Comparison of visual scoring and quantitative planimetry methods for estimation of global infarct size on delayed enhanced cardiac MRI and validation with myocardial enzymes. *Eur. J. Radio.* **78**, 87–92 (2011).
11. Zhang, L. et al. Myocardial infarct sizing by late gadolinium-enhanced MRI: Comparison of manual, full-width at half-maximum, and n-standard deviation methods. *J. Magn. Reson. Imaging* **44**, 1206–1217 (2016).
12. Holtackers, R. J. et al. Dark-blood late gadolinium enhancement cardiovascular magnetic resonance for improved detection of subendocardial scar: a review of current techniques. *J. Cardiovasc. Magn. Reson.* **23**, 1–18 (2021).
13. Liu, C. Y., Wieben, O., Brittain, J. H. & Reeder, S. B. Improved delayed enhanced myocardial imaging with T2-prep inversion recovery magnetization preparation. *J. Magn. Reson. Imaging* **28**, 1280–1286 (2008).
14. Kellman, P. et al. Dark blood late enhancement imaging. *J. Cardiovasc. Magn. Reson.* **18**, 1–11 (2016).
15. Kim, H. W. et al. Dark-blood delayed enhancement cardiac magnetic resonance of myocardial infarction. *JACC Cardiovasc. Imaging* **11**, 1758–1769 (2018).
16. Sridi, S. et al. Improved myocardial scar visualization with fast free-breathing motion-compensated black-blood T1-rho-prepared late gadolinium enhancement MRI. *Diagn. Inter. Imaging* **103**, 607–617 (2022).
17. Fahmy, A. S. et al. Gray blood late gadolinium enhancement cardiovascular magnetic resonance for improved detection of myocardial scar. *J. Cardiovasc. Magn. Reson.* **20**, 1–11 (2018).
18. Holtackers, R. J., Chiribiri, A., Schneider, T., Higgins, D. M. & Botnar, R. M. Dark-blood late gadolinium enhancement without additional magnetization preparation. *J. Cardiovasc. Magn. Reson.* **19**, 1–10 (2017).
19. Francis, R. et al. Prospective comparison of novel dark blood late gadolinium enhancement with conventional bright blood imaging for the detection of scar. *J. Cardiovasc. Magn. Reson.* **19**, 1–12 (2017).
20. Ding, W. et al. Aligning multi-sequence. *CMR Towards Fully Autom. Myocard. Pathol. Segmentation* **XX**, 1–14 (2020).
21. Wei, D., Sun, Y., Chai, P., Low, A. & Ong, S. H. Myocardial segmentation of late gadolinium enhanced MR images by propagation of contours from cine MR images. 1–8 https://doi.org/10.1007/978-3-642-23626-6_53 (2022).
22. Chen, C. et al. Deep learning for cardiac image segmentation: a review. *Front. Cardiovasc. Med.* **7**, 25 (2020).
23. Ruijsink, B. et al. Fully automated, quality-controlled cardiac analysis from CMR: validation and large-scale application to characterize cardiac function. *JACC Cardiovasc. Imaging* **13**, 684–695 (2020).
24. Isensee, F. et al. Automatic cardiac disease assessment on cine-MRI via time-series segmentation and domain specific features. in *Statistical Atlases and Computational Models of the Heart. ACDC and MMWHS Challenges*. Lecture Notes in Computer Science, Vol. 10663, 120–129 (Springer, 2018).
25. Kurzendorfer, T. et al. Myocardial scar segmentation in LGE-MRI using fractal analysis and random forest classification. In *Proc. 24th International Conference on Pattern Recognition (ICPR)* 3168–3173 https://doi.org/10.1109/ICPR.2018.8545636 (2018).
26. Popescu, I. A., Irving, B., Borlotti, A., Dall'Armellina, E. & Grau, V. Myocardial scar quantification using SLIC supervoxels-parcellation based on tissue characteristic strains. in: *Statistical Atlases and Computational Models of the Heart Imaging and Modelling Challenges* (eds Mansi, T. et al.). Lecture Notes in Computer Science, Vol 10124, 182–190 (Springer, 2017).
27. Tao, Q. et al. Automated segmentation of myocardial scar in late enhancement MRI using combined intensity and spatial information. *Magn. Reson. Med.* **64**, 586–594 (2010).
28. Lintingre, P.-F. F. et al. High-resolution late gadolinium enhancement magnetic resonance for the diagnosis of myocardial infarction with nonobstructed coronary arteries. *JACC Cardiovasc. Imaging* **13**, 1135–1148 (2020).
29. Neilan, T. G. et al. CMR quantification of myocardial scar provides additive prognostic information in nonischemic cardiomyopathy. *JACC Cardiovasc. Imaging* **6**, 944–954 (2013).
30. Karim, R. et al. Evaluation of current algorithms for segmentation of scar tissue from late gadolinium enhancement cardiovascular magnetic resonance of the left atrium: an open-access grand challenge. *J. Cardiovasc. Magn. Reson.* **15**, 1–17 (2013).

31. Haïssaguerre, M. et al. Localized structural alterations underlying a subset of unexplained sudden cardiac death. *Circ. Arrhythm. Electrophysiol.* **11**, 1–12 (2018).
32. Bustin, A. et al. High-resolution free-breathing late gadolinium enhancement cardiovascular magnetic resonance to diagnose myocardial injuries following COVID-19 infection. *Eur. J. Radio.* **144**, 109960 (2021).
33. Zeilinger, M. G. et al. 3D Dixon water-fat LGE imaging with image navigator and compressed sensing in cardiac MRI. *Eur. Radio.* **31**, 3951–3961 (2021).
34. Sung, E. et al. Fat infiltration in the infarcted heart as a paradigm for ventricular arrhythmias. *Nat. Cardiovasc. Res.* **1**, 933–945 (2022).
35. Bustin, A. et al. Endogenous assessment of myocardial injury with single-shot model-based non-rigid motion-corrected T1 rho mapping. *J. Cardiovasc. Magn. Reson.* **23**, 1–14 (2021).
36. Griswold, M. A. et al. Generalized autocalibrating partially parallel acquisitions (GRAPPA). *Magn. Reson. Med.* **47**, 1202–1210 (2002).
37. Maillot, A. et al. Automated inversion time selection for black-blood late gadolinium enhancement cardiac imaging in clinical practice. *Magn. Reson. Mater. Phys. Biol. Med.* **36**, 877–885 (2023).
38. de Villedon de Naide, V. et al. Fully automated contrast selection of joint bright- and black-blood late gadolinium enhancement imaging for robust myocardial scar assessment. *Magn. Reson. Imaging* **109**, 256–263 (2024).
39. Dosovitskiy, A. et al. An image is worth 16X16 words: transformers for Image recognition at scale. In *Proc. 9th International Conference on Learning Representations* (ICLR, 2021).
40. Gao, Y. et al. A data-scalable transformer for medical image segmentation: architecture, model efficiency, and benchmark. Preprint at https://doi.org/10.48550/arXiv.2203.00131 (2022).
41. Shamshad, F. et al. Transformers in medical imaging: a survey. *Med. Image Anal.* **88**, 102802 (2023).
42. Xue, H. et al. Landmark detection in cardiac MRI by using a convolutional neural network. *Radiol. Artif. Intell.* **3**, e200197 (2021).
43. Ronneberger, O., Fischer, P. & Brox, T. U-net: convolutional networks for biomedical image segmentation. in *Medical Image Computing and Computer-Assisted Intervention–MICCAI 2015* (eds Navab, N., Hornegger, J., Wells, W., Frangi, A). Lecture Notes in Computer Science, Vol. 9351, 234–241 (Springer, 2015).
44. Cerqueira, M. D. et al. Standardized myocardial segmentation and nomenclature for tomographic imaging of the heart: a statement for healthcare professionals from the cardiac imaging. *Circulation* **105**, 539–542 (2002).
45. Selvadurai, B. S. N. et al. Definition of left ventricular segments for cardiac magnetic resonance imaging. *JACC Cardiovasc. Imaging* **11**, 926–928 (2018).
46. Adams, R. & Bischof, L. Seeded Region Growing. *IEEE Trans. Pattern Anal. Mach. Intell.* **16**, 641–647 (1994).
47. Schuijf, J. D. et al. Quantification of myocardial infarct size and transmurality by contrast-enhanced magnetic resonance imaging in men. *Am. J. Cardiol.* **94**, 284–288 (2004).
48. Van Rugge, F. P. et al. Magnetic resonance imaging during dobutamine stress for detection and localization of coronary artery disease: quantitative wall motion analysis using a modification of the centerline method. *Circulation* **90**, 127–138 (1994).
49. Hansen, M. S. & Sørensen, T. S. Gadgetron: an open source framework for medical image reconstruction. *Magn. Reson. Med.* **69**, 1768–1776 (2013).
50. Weigel, M. Extended phase graphs: dephasing, RF pulses, and echoes-pure and simple. *J. Magn. Reson. Imaging* **41**, 266–295 (2015).
51. Captur, G. et al. A medical device-grade T1 and ECV phantom for global T1 mapping quality assurance- the T1 mapping and ECV standardization in cardiovascular magnetic resonance (T1MES) program. *J. Cardiovasc. Magn. Reson.* **18**, 1–20 (2016).
52. Dib, N. et al. A percutaneous swine model of myocardial infarction. *J. Pharm. Toxicol. Methods* **53**, 256–263 (2006).
53. Schulz-Menger, J. et al. Standardized image interpretation and post-processing in cardiovascular magnetic resonance-2020 update: Society for Cardiovascular Magnetic Resonance (SCMR) Board of Trustees Task force on standardized post processing. *J. Cardiovasc. Magn. Reson.* **22**, 19 (2020).
54. Dice, L. R. Measures of the amount of ecologic association between species. *Ecology* **26**, 297–302 (1945).

Acknowledgements

This research was supported by funding from the French National Research Agency under grant agreements Equipex MUSIC ANR-11-EQPX-0030, ANR-21-CE17-0034-01, Programme d'Investissements d'Avenir ANR-10-IAHU04-LIRYC, and ANR Chaire Professeur Junior ANR-22-CPJ2-0009-01. This project has received funding from the European Research Council (ERC) under the European Union's Horizon Europe research and innovation programme (Grant agreement No. 101076351).

Author contributions

Conceptualization: A.B., M.S., and H.C., methodology: A.B., M.S., and H.C., data curation: A.B., H.C., G.M., D.P., T.B., J.M., S.S., C.B., G.D., S.C.G., I.B.L., and M.M., writing–original draft: A.B., M.S., and H.C., writing–review and editing: V.V.N., M.V.M., K.N., T.G., T.R., P.G., V.O., M.C., G.C., K.V., and M.H., funding acquisition: A.B., P.J., M.S., and H.C.

Competing interests

The authors declare no competing interests.

Additional information

Supplementary information The online version contains supplementary material available at https://doi.org/10.1038/s41467-025-66166-0.

Correspondence and requests for materials should be addressed to Aurelien Bustin.

Peer review information *Nature Communications* thanks Steven Cho and Michael Jerosch-Herold for their contribution to the peer review of this work. A peer review file is available.